Nanoscale

ROYAL SOCIETY OF CHEMISTRY

PAPER

View Article Online
View Journal

Check for updates

Cite this: DOI: 10.1039/d6nr00687f

Single-molecule detection of amino acid phosphorylation using electron tunnelling currents: toward neurodegenerative disease diagnosis

Yuki Komoto,[a,b] Wataru Takahagi,[c] Takahito Ohshiro,[a,b] Sumire Nishihata,[d] Kosuke Fujishima[c,e] and Masateru Taniguchi *[a]

Received 16th February 2026,
Accepted 28th April 2026

DOI: 10.1039/d6nr00687f

rsc.li/nanoscale

Protein phosphorylation is one of the most prevalent post-translational modifications regulating biological functions, and its dysregulation is closely associated with neurodegenerative diseases such as Alzheimer's and Parkinson's disease. Despite extensive studies, direct detection of phosphorylation at the single-molecule level remains challenging because conventional mass spectrometry and antibody-based assays require complex pretreatments and cannot comprehensively resolve site-specific modifications. To address this challenge, we employed mechanically controllable break junction (MCBJ) measurements to probe the single-molecule conductance of serine (Ser), threonine (Thr), tyrosine (Tyr), and their phosphorylated counterparts. Distinct conductance trends were observed depending on the amino acid species, reflecting the influence of phosphate substitution on the electronic states. Density functional theory (DFT) calculations revealed that phosphorylation-induced shifts in HOMO levels and changes in π-conjugation account for the observed conductance variations. Furthermore, statistical analysis combined with machine-learning-based classification enabled discrimination between phosphorylated and non-phosphorylated amino acids with high accuracy, demonstrating that single-molecule electrical signals contain sufficient molecular information for identifying phosphorylation. This study establishes an electronic readout approach for amino acid phosphorylation and provides a proof of concept for extending single-molecule electrical techniques toward quantitative and sequencing-oriented analyses of protein modifications.

1 Introduction

The accumulation of abnormally post-translationally modified proteins is implicated in the onset of neurodegenerative diseases such as Alzheimer's and Parkinson's disease.[1–7] Among various post-translational modifications (PTMs), phosphorylation has attracted considerable attention. The introduction of phosphate groups into amino acids bearing hydroxyl groups—namely serine (Ser), threonine (Thr), and tyrosine (Tyr)—can alter protein structure and solubility, and thus has been extensively studied to better understand disease mechanisms and to develop therapeutic strategies. For example, in Alzheimer's disease, excessive phosphorylation of Ser and Thr residues in the microtubule-associated tau protein reduces its affinity for microtubules, resulting in the intracellular accumulation of tau.[6] While Ser phosphorylation has long been the primary focus in neurodegenerative disorders, recent studies have also revealed that Tyr phosphorylation contributes to disease progression.[8,9] Although phosphorylation at a single site may have little effect, multiple concurrent phosphorylation events can sometimes lead to substantial changes in a protein's aggregation propensity.[7] Therefore, evaluating phosphorylation at multiple amino-acid residues is crucial for understanding neurodegenerative pathogenesis. Mass spectrometry (MS) and antibody-based assays have traditionally been employed for detecting protein phosphorylation.[10–12] Although MS enables highly sensitive identification, phosphorylated peptides are typically of low abundance and exhibit poor ionization efficiency, necessitating complicated pretreatment steps such as enrichment and purification.[10] Furthermore,

---

[a] *SANKEN, The University of Osaka, 8-1, Mihogaoka, Ibaraki, Osaka 567-0047, Japan. E-mail: komoto@sanken.osaka-u.ac.jp*
[b] *Artificial Intelligence Research Center, Osaka University, 8-1 Mihogaoka, Ibaraki, Osaka 567-0047, Japan*
[c] *Earth-Life Science Institute, Institute of Science Tokyo, 2-12-1 Ookayama, Meguro-ku, Tokyo 152-8550, Japan*
[d] *St. Andrew's Senior High School, 1-1, Manabino, Izumi, Osaka 594-1198, Japan*
[e] *Graduate School of Media and Governance, Keio University, 5322 Endo, Fujisawa, Kanagawa 252-0816, Japan*

positionally isomeric phosphopeptides are difficult to distinguish.[13] Antibody-based methods, on the other hand, are effective for specific targets but are limited by the difficulty of producing antibodies that specifically recognize phosphorylated residues, making comprehensive analyses challenging.

To overcome these limitations, we focused on single-molecule electrical measurements as a new approach for detecting phosphorylation. In this technique, a metallic nanowire fabricated by nanolithography is mechanically broken to form a nanometer-scale gap electrode, through which the current mediated by individual molecules can be directly measured.[14–16] Using single-molecule measurements, conductance has been previously characterized for nucleic acids,[17–19] amino acids,[20,21] phosphorylated tyrosine,[20] and phosphorylated peptide.[22] This approach is therefore expected to be applicable to the simultaneous identification of phosphorylated amino acids, including serine and threonine, which are of particular interest in disease studies.[7,8] Recent studies have shown that applying machine-learning algorithms to single-molecule signals can improve the discrimination accuracy.[21,23–25] In this study, we developed a method for distinguishing phosphorylation at the single-residue level by combining single-molecule electrical measurements with machine learning. While the present work is limited to individual amino acids, it provides a proof-of-concept for extending this approach to more complex peptide systems, including the potential identification of multi-site phosphorylation in the future. In addition to sequence analysis, detection of phosphorylated serine as a potential biomarker.[26] Detecting phosphorylation events at the single-residue level provide a basis for developing novel, simple diagnostic technologies.

We performed mechanically controllable break junction (MCBJ) measurements in aqueous solutions of serine (Ser), threonine (Thr), tyrosine (Tyr), phosphoserine (pSer), phosphothreonine (pThr), and phosphotyrosine (pTyr), as shown in Fig. 1.

2 Method

2.1 Sample preparation

L-Serine (TCI, ≥99%), L-(−)-threonine (TCI, ≥99%), L-(−)-tyrosine (TCI, ≥98.5%), *O*-phospho-L-serine (Sigma-Aldrich, ≥98%), *O*-phospho-L-threonine (Cayman, ≥95%), and *O*-phospho-L-tyrosine (TCI, ≥97%) were dissolved in MillQ water to prepare a 1 μM solution.

2.2 Device fabrication

Schematic structure of MCBJ device is shown in Fig. 1. Polyimide film was coated as an insulating layer onto thin-silicon substrate with spin coating. A gold nanowire was drawn on the silicon substrate by electron-beam lithography. Then, SiO_2 film was coated on the gold nanowire by chemical vapor deposition. Narrowest part of nanowire is several ten nm. Polyimide layer under gold nanowire were removed by dry-etching to form free-standing gold-wire.[21] The PDMS pool for solution containment was attached onto the substrate as described in SI.

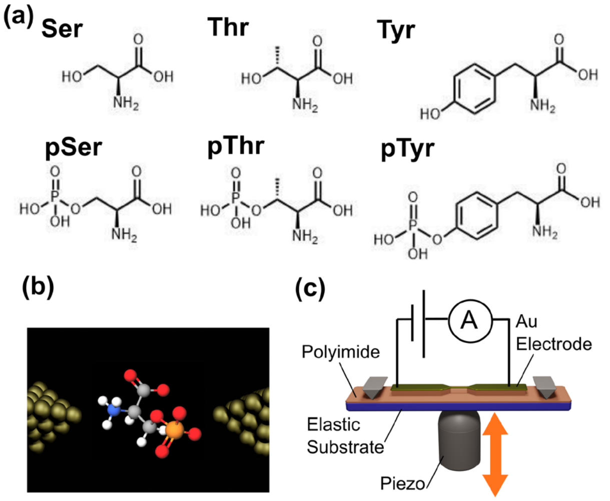

Fig. 1 (a) Chemical structures of target molecules, Ser, pSer, Thr, pThr, Tyr, pTyr. (b) Schematic view of single-molecule measurement of pSer. (c) Schematic view of MCBJ set-up.

2.3 Electrical measurement

Single-molecule conductance measurements were performed as described in previous reports.[21] A lithographically fabricated gold nanowire on a thin silicone substrate was broken by mechanically bending the substrate under ambient condition with application of a bias voltage of 100 mV, and the single detection part of the nanogap electrodes was formed. Throughout the junction breaking process, the junction conductance (G) was monitored using a picoammeter (Keithley 6487). A series of conductance jumps of the order of $G_0 = 2e^2/h$ (where e and h are the elementary charge and Planck's constant, respectively) was observed, and the final conductance was $1G_0$. Several seconds after reaching the $1G_0$ state, a gold atomic junction naturally ruptured in the nanowire, creating a nanogap. The gap size was controlled using the piezo bias voltage. The gap width was 0.56 and 0.58 nm. The gap distance was estimated from the baseline tunnelling current as described in SI.

2.4 Theoretical calculation

Density functional theory (DFT) calculations[27,28] were performed at the long-range-corrected hybrid functional level for the molecules in an aqueous solution in order to accurately evaluate the highest occupied molecular orbital (HOMO) energy, which serves as a key indicator of molecular conductance. The initial three-dimensional structures were sketched in ChemDraw 23.1.1 and converted to Cartesian coordinates. The ground-state structures were calculated as singlet zwitterions, with net charges of 0 for the non-phosphorylated residues (Ser, Thr, and Tyr) and −2 for the phosphorylated residues (pSer, pThr, and pTyr). A preliminary geometry refinement was then performed with the Universal Force Field (UFF)[29] as implemented in Avogadro 1.2.0[30] to remove severe steric clashes. Subsequent quantum-chemical calculations were carried out on the TSUBAME 4.0 supercomputing system at Institute of Science Tokyo using Gaussian 16 Rev. C.02.[31] Geometry optimizations and frequency analyses were carried out at the long-range-corrected hybrid DFT level, ωB97X-D/def2-TZVPP[32–34] incorporating bulk aqueous effects through the IEFPCM continuum model.[35] Subsequent geometry optimizations and frequency analyses were carried out at the ωB97X-D/def2-TZVPP level with SMD implicit-solvation model; the absence of imaginary frequencies verified that all structures correspond to true minima.[36] Finally, single-point energies were evaluated on the optimized geometries using the larger def2-QZVPP basis set at the same ωB97X-D level.

2.5 Machine learning identification

XGBoost classifier in scikit-learn library was used to machine learning analysis. Default hyper parameters of random forest classifier was adopted. The analysis was performed using Python 3.10.9 with scikit-learn library version 1.2.1 and xgboost library version 1.7.5.

3 Results and discussion

Fig. 2 shows the current-time profiles obtained for each molecule. Fig. 2(a, c, e, g, i and k) shows the current traces recorded over 300 s. Pulsatile current signals were observed for all amino acids and phosphorylated amino acids at a higher frequency compared to the blank measurement shown in SI 3. Fig. 2(b, d, f, h, j and l) present enlarged views of representative pulse signals. In previous single-molecule measurements of amino acids, rectangular-shaped pulse signals were predominantly observed. The results obtained in the present study are consistent with those reported in studies on amino acid measurements. For all molecules, the frequent appearance of such signals compared with the blank measurements supports that the observed pulses originate from the target molecules. Both phosphorylated and non-phosphorylated amino acids were successfully detected at the single-molecule level, demonstrating the potential of this approach for single-molecule discrimination of amino acid phosphorylation.

It is well known that signals obtained from single-molecule measurements inherently exhibit variability in conductance due to differences in molecular orientation and electrode structure.[37,38] Therefore, it is difficult to discuss the characteristics of single-molecule conductance based solely on individual signals, and a statistical analysis of all pulse signals is required. Table 1 summarizes the average conductance of the maximum current values (I_p) for each amino acid. I_p was defined as the maximum current of each pulse signal as shown in Fig. S3 in SI. For Ser and Thr, a decrease in average conductance was observed upon phosphorylation, whereas Tyr exhibited an increase in conductance after phosphorylation.

To further analyze signal variations beyond the mean values, the histograms of the maximum current I_p and the two-dimensional histograms of I_p *versus* the duration of the pulse (T_d) are shown in Fig. 3(a–f). The high-conductance signals decreased upon phosphorylation for Ser and Thr, whereas they increased for Tyr. However, the statistical differences in signal distributions between phosphorylated and non-phosphorylated species were small, and the histograms largely overlapped. To better visualize the subtle changes induced by phosphorylation, we conducted an additional analysis. Fig. 3(g–i) show differences in probability density between phosphorylated and non-phosphorylated amino acids. In this analysis, probability density maps were obtained

Table 1 Average I_p/pA and T_d/ms

Amino acid	I_p/pA	T_d/ms
Ser	36	6.0
pSer	34	4.4
Thr	33	5.6
pThr	26	4.6
Tyr	34	4.3
pTyr	38	4.0

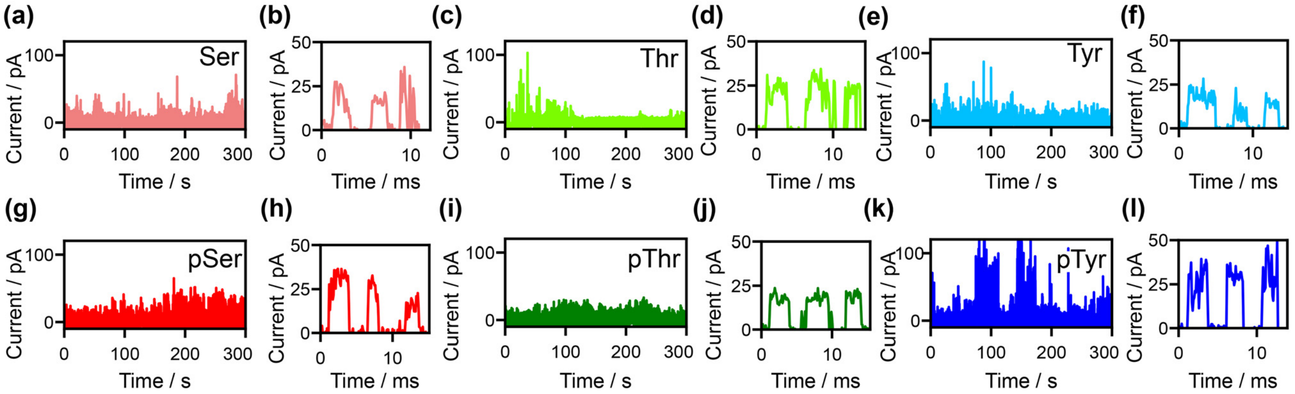

Fig. 2 Current–time profiles of single-amino acid measurements. (a, c, e, g, i and k) Raw current traces for the entire measurement period. (b, d, f, h, j and l) Enlarged views of single-molecule pulse signals. (a, b), (c, d), (e, f), (g, h), (i, j), and (k, l) correspond to Ser, Thr, Tyr, pSer, pThr, and pTyr, respectively. The electrical measurements were performed under bias voltage with 100 mV.

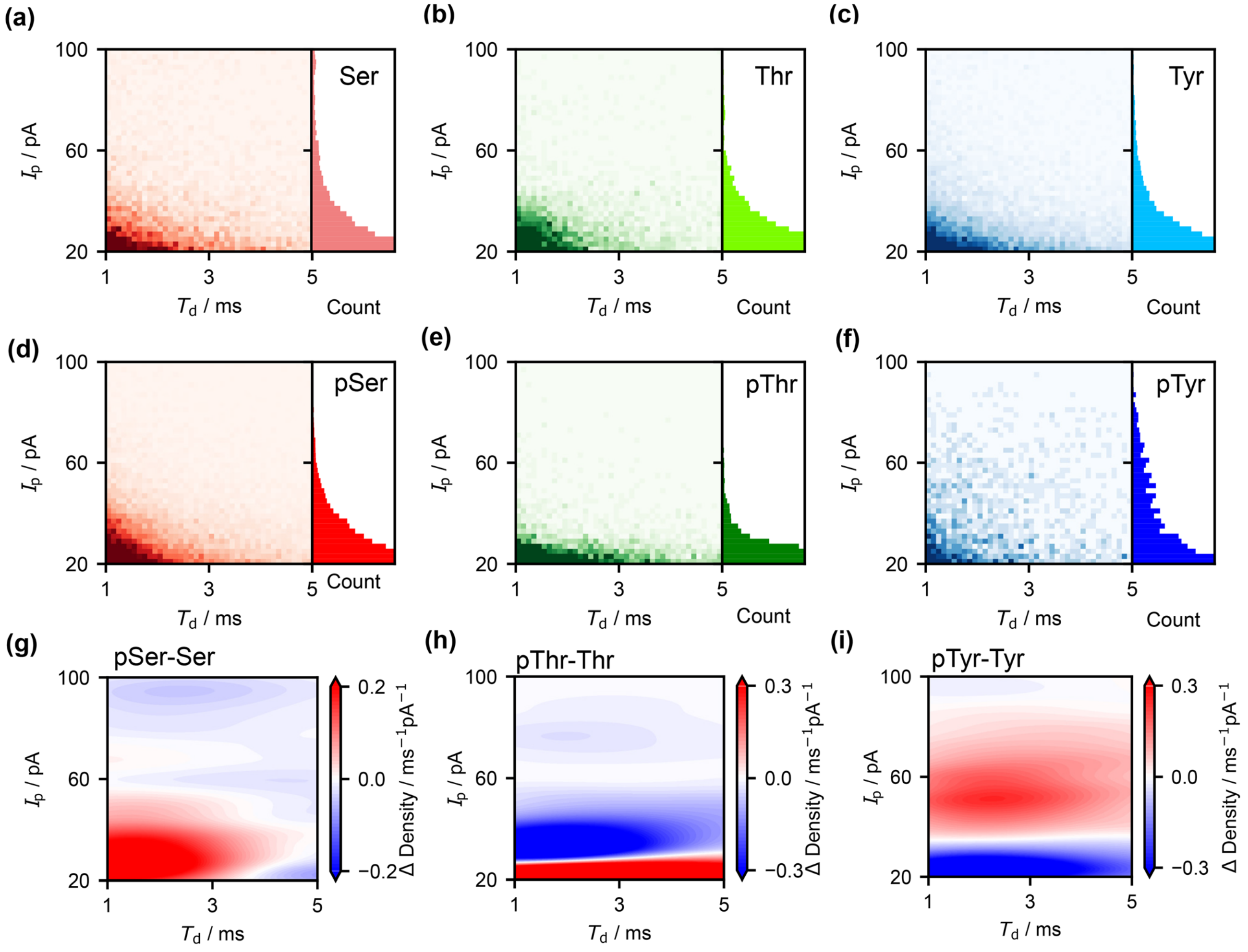

Fig. 3 Statistical analysis of single-molecule current pulses. (a–f) I_p–T_d 2D histogram and I_p histograms of Ser, Thr, Tyr, pSer, pThr, and pTyr, for (a–f), respectively. I_p and T_d represent maximum current of the signal and signal duration time. (g–i) Difference of probability densities between amino acid and phosphorylated amino acid. Positive values indicate a higher occurrence of phosphorylated amino acids.

using kernel density estimation (KDE) for both amino acids and their phosphorylated counterparts. KDE estimates the overall probability density by summing Gaussian kernels placed on the observed data points. By subtracting the density map of amino acids from that of phosphorylated amino acids, we can identify regions where one species appears more frequently than the other. In Fig. 3(g–i), positive values (red) indicate regions where phosphorylated amino acids are observed more frequently, while negative values (blue) correspond to regions where non-phosphorylated amino acids are more likely to appear. These heat maps reveal that, upon phosphorylation, the probability density increases in the low-conductance region for Ser and Thr, whereas it increases in the high-conductance region for Tyr. Thus, the probability density analysis based on KDE supports the same trend as observed in the average conductance results.

Single-molecule measurements revealed conductance changes upon phosphorylation (Fig. 2). Charge transport in a molecular junction depends critically on the energy alignment of the transport orbitals relative to the Fermi level of the Au electrode ($E_F \approx -5.31$) and on the electrode–molecule coupling Γ. In general, better level alignment (smaller $|E_F - \varepsilon|$) and stronger coupling both promote higher conductance, but neither factor alone is sufficient.[16] To interpret the experimental trends, we performed first-principles geometry optimizations and electronic-structure calculations (DFT; details in section 2.4). Fig. 4 shows the frontier orbital energy diagram. The HOMO of Ser and Thr resides mainly on the carboxylate group (−9.474 eV and −9.455 eV), while that of Tyr localizes on the aromatic ring (−8.233 eV) (Fig. 5). Upon phosphorylation, the HOMO of pSer/pThr relocates to the phosphate (−8.620 eV and −8.612 eV), *i.e.*, energetically closer to E_F, which would naively suggest higher conductance. Experimentally, however, Ser/Thr show a conductance decrease upon phosphorylation. This indicates that level alignment alone cannot explain the data; one must also consider Γ, which is governed by effective distance, orientation, and interfacial environment. In particular, phosphate anions exhibit strong hydration and pH-depen-

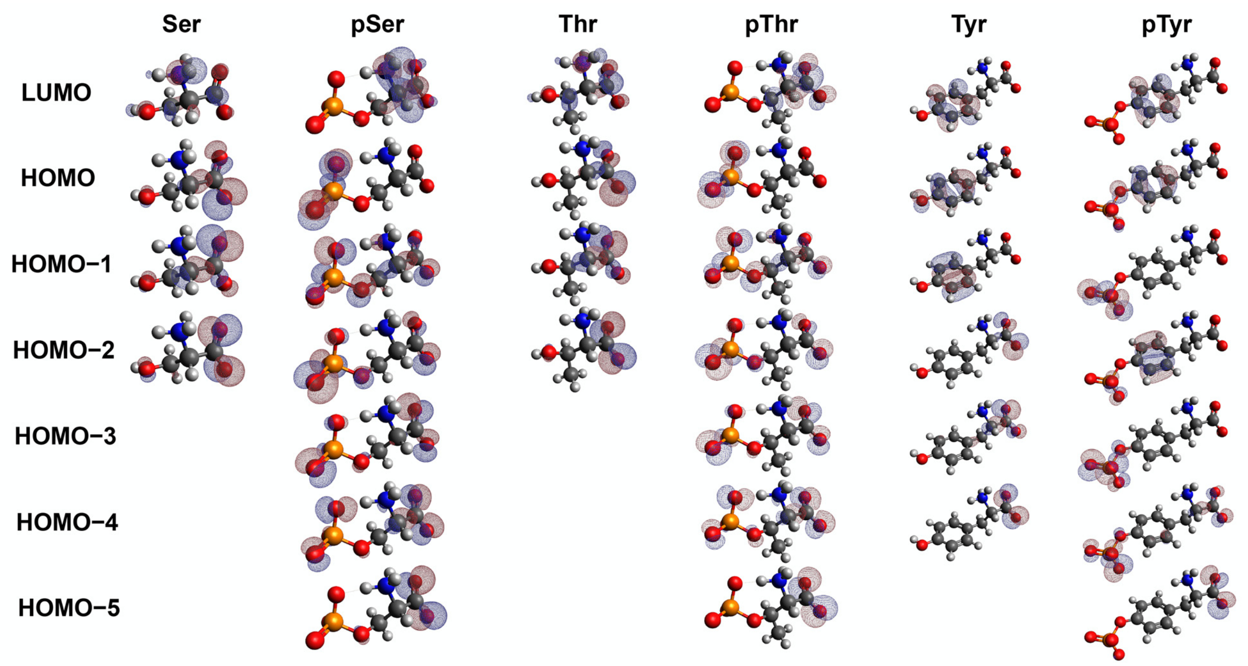

Fig. 4 Isosurface of HOMOs/LUMO of Ser, pSer, Thr, pThr, Tyr, and pTyr calculated by DFT ωB97X-D/def2-QZVPP//ωB97X-D/def2-TZVPP[32–34] (Isovalue = 0.05). Solvation effects were incorporated with the Solvation Model based on Density (SMD) implicit-solvent model, parameterized for water.

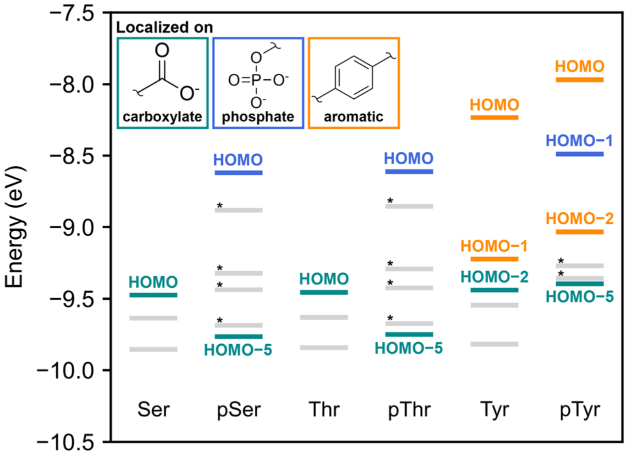

Fig. 5 Schematic energy diagram of HOMOs of Ser, pSer, Thr, pThr, Tyr, and pTyr. The spatial distribution of the HOMOs marked with asterisks is almost evenly split between the phosphate site and the carboxylate sites (see Fig. 4).

dent specific adsorption on Au(111), which restructures the double layer and can weaken the contact (reduce Γ).[39] Consistent with this model, the HOMO through HOMO−4 orbitals of pSer/pThr are localised on the phosphate (Fig. 4).

Single-molecule conductance is commonly associated with frontier molecular orbitals. However, molecular conductance is not exclusively determined by orbital energy alignment; the strength and nature of electrode–molecule coupling also play a significant role.[40] Typically, such efficient coupling between a molecular orbital and the electrode is established *via* strong covalent anchoring groups such as thiols, where the spatially diffuse sulfur 3p orbitals extensively hybridize with the gold electrodes to form broadened, highly transparent transport channels.[41,42] In contrast, the oxygen 2p orbitals of carboxylate groups exhibit increased spatial contraction, resulting in inherently weaker electronic coupling.[43] In the non-anchored system, the phosphate group, despite possessing high-lying HOMOs, experiences steric hindrance arising from hydration and interfacial electrostatic effects. These factors restrict the physical approach of the group to the electrodes and thereby limit its contribution to tunnelling transport. Consequently, although HOMOs localized on the phosphate group are relatively high in energy, the difficulty in securing close proximity to the electrodes may act to lower Γ. This interpretation suggests transport *via* deeper-lying orbitals as one of the possible mechanisms contributing to the reduced conductance observed in pSer and pThr. Orbitals localized on the carboxylate group, such as the HOMO−5 of pSer and pThr, can be involved in the tunnelling current. Despite the absence of a covalent anchoring group or a conjugated bridge in the molecules, the carboxylate group remains physically accessible and may transiently approach the electrodes. Consequently, HOMO−5 can also function as a possible tunnelling pathway and can contribute to charge transport under dynamic fluctuations. These deeper-lying orbitals are located farther from the Au Fermi level than the HOMO of the non-phosphorylated species as represented in Fig. 5. This energy offset may contribute to the observed decrease in conductance upon phosphorylation.

The LUMOs of pSer and pThr also exhibit spatial distributions localized on the carboxylate group, similar to HOMO−5. However, DFT calculations indicate that these orbitals lie farther from the Fermi level than HOMO−5, as shown in Fig. S3 in SI 4. Their contribution to tunnelling transport is therefore considered to be less significant, although it cannot be excluded entirely.

As an alternative transport mechanism, a decrease in conductance can also be considered even when transport occurs *via* HOMO. The molecular sizes are summarized in Table S1 in SI 5. Phosphorylation can increase the effective tunnelling decay distance, due to both increased molecular length and hydration, thereby reducing conductance. As a result, even for HOMO-mediated transport, the conductance may decrease upon phosphorylation.

By contrast, the increased conductance observed for Tyr upon phosphorylation appears to be related to the HOMO of pTyr localized on the aromatic ring. In pTyr, the aromatic π HOMO usually sits higher than oxygen-centred occupied orbitals because differential solvation stabilizes phosphate/carboxylate lone-pair states far more than the ring π level. In aqueous or other polar media, phosphate (PO_4^{n-}) forms a strong, structured first hydration shell with slowed water dynamics, and carboxylates likewise show pronounced hydration signatures; both effects pull down the energies of n(O)-type occupied orbitals relative to vacuum. By contrast, the hydrophobic phenyl π system couples weakly to the reaction field and is much less downward-stabilized, leaving the ring-centered HOMO relatively higher.[39,44] This solvation asymmetry is compounded by limited π-conjugation across the Ph–O–P linkage: aryl phosphates transmit mostly inductive rather than effective π-resonance into the ring, so the phenyl π level remains close to that of a phenoxy/phenyl unit instead of being pulled down by extended delocalization. Phosphorylation also renders the molecule anionic, which tends to raise all occupied levels on a vacuum scale; however, because oxygen-localized orbitals are preferentially re-stabilized by hydration and hydrogen bonding, the aromatic π HOMO remains the highest after competing shifts are accounted for. For transport, note that conductance depends on level alignment and electrode–molecule coupling Γ, not alignment alone.

The broad conductance distribution reflects contributions from multiple configurations, including those with more effective π-metal interactions as well as configurations where the π-plane is more parallel to the electrodes and through-space tunnelling becomes significant.[45–48]

The results of this experimental and theoretical study suggest that conductance in such dynamic nanogap systems is governed not only by absolute orbital energy alignment but also critically by physical accessibility, spatial orbital distribution, and transient electrode–molecule coupling under fluctuating configurations. The present discussion of transport is necessarily qualitative, as the DFT calculations in this study primarily provide information on energy levels and orbital localization in solution. Therefore, the proposed mechanism should be regarded as a plausible interpretation consistent with the observations. A more complete understanding will require transport calculations that incorporate molecular configurations in solution.

For completeness, we note that earlier single-molecule studies have demonstrated that Tyr and pTyr can be distinguished based on the statistical properties of current pulses. In our measurements, the observed current signals do not arise from transport through stable molecular junctions, but rather from stochastic tunnelling events mediated by transient molecular configurations within the nanogap. This behavior is conceptually related to both recognition tunnelling approaches[49] and prior research.[20] Similar to previous method,[20] and unlike recognition tunnelling methods,[49] our system does not utilize any recognition molecules. The measured conductance originates from probabilistic tunnelling through temporarily oriented molecules. However, despite the presence of orientational freedom, this study differs from previous work[20] in that a narrower nanogap is employed. This spatial confinement is expected to restrict the accessible molecular configurations, thereby influencing the observed current distributions. Therefore, the measured signals should be interpreted not as steady-state molecular conductance, but as configuration-dependent tunnelling events under spatial confinement. The conductance behavior observed in this study differs from ref. 20, and thus direct up/down comparisons should be made with care. Theoretical studies show that phosphorylation affects conductance increase/decrease, consistent with our observations.[50] In these models, the phosphate group may directly participate in the transport pathway. The lower observed conductance supports the interpretation that coupling is weaker and configuration-dependent in our solvated and transient conduction system. The phosphate group is more likely to influence conductance indirectly. This interpretation is supported by recent work emphasizing the role of molecular configuration.[51] Overall, our DFT results corroborate that single-molecule conductance captures molecule-intrinsic features, while also emphasizing that the transport orbital closest to E_F is not necessarily the dominant channel; interfacial coupling Γ can be equally decisive. Moreover, solvent/double-layer effects and surface chemistry modulate transport systematically, as highlighted in recent measurements.[52]

Changes in conductance were observed in the single-molecule measurements, and these experimentally observed variations could be rationalized by the DFT calculations. However, the distributions of the peak current and signal duration were broad, and the corresponding histograms showed substantial overlap. Therefore, it was not possible to identify each molecule solely from the peak current or duration of a single signal. To overcome this limitation, we applied a machine learning-based classification approach, which has been reported to enhance molecular discrimination in various single-molecule systems, to achieve identification at the single-molecule level.[21,23] Fig. 6(a) illustrates the classification scheme. Current traces were recorded using the MCBJ tech-

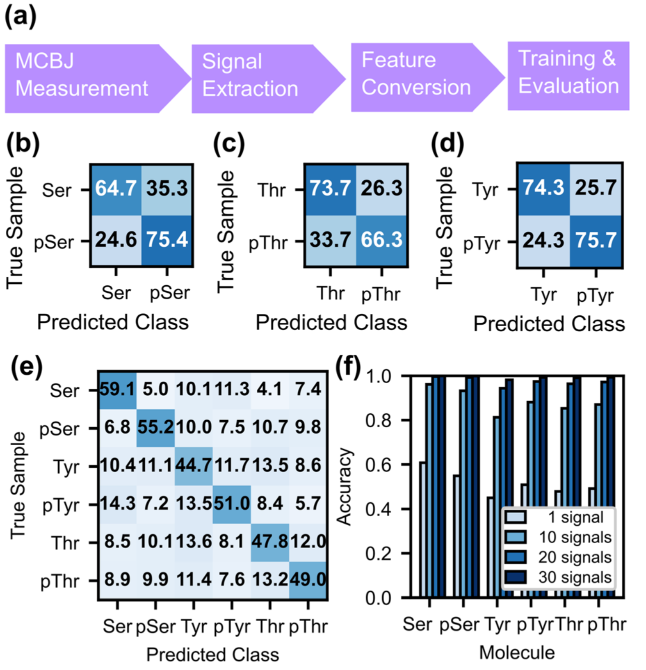

Fig. 6 (a) Classification scheme for single-molecule signals discrimination. (b–e) Confusion matrices of classification between Ser and pSer (b), Thr and pThr (c), Tyr and pTyr (d) among Ser, pSer, Thr, pThr, Tyr, and pTyr (e).(f) Classification accuracy for each amino acid obtained by majority-voting over multiple signals.

nique, and pulse-like signals were extracted. Each extracted signal was converted into a 15-dimensional feature vector consisting of the peak current (I_p), pulse duration (T_d), average current, and 12 averaged shape factors normalized by I_p obtained through average pooling as shown in Fig. S4 in SI. These features were used for training and testing with 10-fold cross-validation. A random forest classifier was employed for discrimination. The classification results for the phosphorylated and non-phosphorylated forms of each amino acid are shown in Fig. 6(b–d). The classification accuracies were 0.70, 0.79, and 0.75 for Ser, Thr, and Tyr, respectively. The highest accuracy was achieved for Tyr, which exhibited a pronounced increase in high-conductance signals upon phosphorylation. The same classification procedure was also applied to discriminate among all six molecules. The results are shown in Fig. 6(e). In all cases, the correct class was predicted with the highest frequency, and the overall six-class classification accuracy was 0.51. Considering that random classification would yield an accuracy of 0.16, the classification of amino acids and their phosphorylated forms was successfully achieved. Feature importances analysis of the classification model was performed (see SI 6). The results show that the I_p and the average current contribute most significantly to the classification, confirming that differences in conductance are the primary factors governing discrimination. Fig. 6(f) summarizes the classification accuracy obtained by integrating multiple signals based on the confusion matrix in Fig. 6(e). By applying a majority-voting scheme described in SI 7 to 10 individual signals, an average classification accuracy of 0.88 was achieved. Increasing the number of integrated signals further improved the accuracy to 0.97 for 20 signals and 0.99 for 30 signals. For 30 signals, the accuracies of Ser and pSer are over 0.999. These classification accuracies are achieved through the accumulation of multiple signals; therefore, reliable discrimination requires the integration of multiple events rather than relying on single-event measurements. These results demonstrate that single-molecule measurements enable reliable discrimination between amino acids and their phosphorylated forms.

4 Conclusions

In summary, we successfully obtained single-molecule conductance signals for Ser, Thr, Tyr, and their phosphorylated counterparts using MCBJ measurements. Upon phosphorylation, the conductance decreased for Ser and Thr, whereas it increased for Tyr. It was shown that changes in conductance depend on the conjugated nature of the carbon atoms to which phosphate groups are bound. The observed conductance changes cannot be explained solely by the HOMO level alignment. Instead, DFT calculations indicate that, for serine and threonine, phosphorylation leads to a redistribution of orbitals, including shifts in orbitals localized on the carboxylate group, which contribute to the transport channels. In contrast, for tyrosine, the conductance change is associated with a shift and enhanced contribution of orbitals localized on the aromatic ring. The single-molecule measurements captured differences in the intrinsic molecular characteristics. The results of this study suggest that characteristic features of amino acids can be distinguished even in stochastic junctions, underscoring the robustness of the present framework. This represents an important step toward understanding charge transport mechanisms in dynamically fluctuating nanogap systems. Furthermore, by applying machine learning-based classification, we achieved successful discrimination of phosphorylated amino acids at the single-molecule level. These findings are expected to provide the basis for developing a simple method for quantifying phosphorylation of serine and threonine, and ultimately for establishing a technique capable of reading phosphorylation modifications at the single-molecule level in future amino acid sequencing.

Author contributions

Conceptualization, Y. K., T. O. and M. T.; experiment, Y. K., T. O. and S. N.; analysis, Y. K. and T. O.; calculation, W. T.; visualization, Y. K. and W. T.; writing – original draft, Y. K. and W. T.; writing – review and editing, Y. K., W. T., T. O., K. F. and M. T. All authors have approved the final version of the manuscript.

Conflicts of interest

There are no conflicts to declare.

Data availability

The data supporting this article have been included as part of the supplementary information (SI). Data and codes for this article are available at Zenodo at https://doi.org/10.5281/zenodo.17889934.

Supplementary information is available. See DOI: https://doi.org/10.1039/d6nr00687f.

Acknowledgements

This work was partly supported by the Japan Society for the Promotion of Science (JSPS)/Ministry of Education, Culture, Sports, Science and Technology (MEXT) KAKENHI Grant Numbers 24K08201, 23K21064, 25H01060, 24K10680, JST K Program Grant Number JPMJKP23H3, Japan, The University of Osaka, Science and Engineering Enhanced Education for Distinguished Students (SEEDS) program and the Human Frontier Science Program (HFSP) Grant Number RGEC27/2023. Quantum chemical calculations were carried out using the TSUBAME4.0 supercomputer at Institute of Science Tokyo. The authors gratefully acknowledge the anonymous reviewers for their helpful and constructive comments, which have greatly improved the quality of this manuscript.

References

1 C. Sexton, H. Snyder, D. Beher, A. L. Boxer, P. Brannelly, J.-P. Brion, L. Buée, A. M. Cacace, G. Chételat, M. Citron, S. L. DeVos, K. Diaz, H. H. Feldman, B. Frost, A. M. Goate, M. Gold, B. Hyman, K. Johnson, C. M. Karch, D. R. Kerwin, W. J. Koroshetz, I. Litvan, H. R. Morris, C. J. Mummery, J. Mutamba, M. C. Patterson, Y. T. Quiroz, G. D. Rabinovici, A. Rommel, M. B. Shulman, L. M. Toledo-Sherman, S. Weninger, K. R. Wildsmith, S. L. Worley and M. C. Carrillo, *Alzheimers Dement*, 2022, **18**, 988–1007.

2 C. Salazar and T. Höfer, *FEBS J.*, 2009, **276**, 3177–3198.

3 J. Wu, J. Wu, T. Chen, J. Cai and R. Ren, *Neurochem. Int.*, 2024, **180**, 105880.

4 W. Li, H.-L. Li, J.-Z. Wang, R. Liu and X. Wang, *Cell Biosci.*, 2024, **14**, 22.

5 J. Berlanga-Acosta, G. Guillén-Nieto, N. Rodríguez-Rodríguez, M. L. Bringas-Vega, D. García-del-Barco-Herrera, J. O. Berlanga-Saez, A. García-Ojalvo, M. J. Valdés-Sosa and P. A. Valdés-Sosa, *Front. Endocrinol.*, 2020, **11**, 560375.

6 A. d. C. Alonso, I. Grundke-Iqbal and K. Iqbal, *Nat. Med.*, 1996, **2**, 783–787.

7 Y. Xia, S. Prokop and B. I. Giasson, *Mol. Neurodegener.*, 2021, **16**, 37.

8 J. Kim, B. Tadros, Y. H. Liang, Y. Kim, C. Lasagna-Reeves, J. Y. Sonn, D.-e. C. Chung, B. Hyman, D. M. Holtzman and H. Y. Zoghbi, *Nat. Neurosci.*, 2024, **27**, 2417–2429.

9 S. Guha, G. V. W. Johnson and K. Nehrke, *Mol. Neurobiol.*, 2020, **57**, 5103–5120.

10 A. N. Polat and N. Özlü, *Analyst*, 2014, **139**, 4733–4749.

11 C. Solier and H. Langen, *Proteomics*, 2014, **14**, 774–783.

12 H. Voshol, M. Ehrat, J. Traenkle, E. Bertrand and J. van Oostrum, *FEBS J.*, 2009, **276**, 6871–6879.

13 G. Muneer, C.-S. Chen and Y.-J. Chen, *Proteomics*, 2025, **25**, e202400087.

14 E. M. Dief, P. J. Low, I. Díez-Pérez and N. Darwish, *Nat. Chem.*, 2023, **15**, 600–614.

15 A. Vezzoli, *Nanoscale*, 2022, **14**, 2874–2884.

16 F. Evers, R. Korytár, S. Tewari and J. M. van Ruitenbeek, *Rev. Mod. Phys.*, 2020, **92**, 035001.

17 M. Di Ventra and M. Taniguchi, *Nat. Nanotechnol.*, 2016, **11**, 117–126.

18 M. Zwolak and M. Di Ventra, *Rev. Mod. Phys.*, 2008, **80**, 141–165.

19 T. Ohshiro, M. Konno, A. Asai, Y. Komoto, A. Yamagata, Y. Doki, H. Eguchi, K. Ofusa, M. Taniguchi and H. Ishii, *Sci. Rep.*, 2021, **11**, 19304.

20 T. Ohshiro, M. Tsutsui, K. Yokota, M. Furuhashi, M. Taniguchi and T. Kawai, *Nat. Nanotechnol.*, 2014, **9**, 835–840.

21 Y. Komoto, T. Ohshiro, Y. Notsu and M. Taniguchi, *RSC Adv.*, 2024, **14**, 31740–31744.

22 T. Harashima, Y. Egami, K. Homma, Y. Jono, S. Kaneko, S. Fujii, T. Ono and T. Nishino, *J. Am. Chem. Soc.*, 2022, **144**, 17449–17456.

23 Y. Komoto, J. Ryu and M. Taniguchi, *Chem. Commun.*, 2023, **59**, 6796–6810.

24 W. Bro-Jørgensen, J. M. Hamill, R. Bro and G. C. Solomon, *Chem. Soc. Rev.*, 2022, **51**, 6875–6892.

25 T. Fu, Y. Zang, Q. Zou, C. Nuckolls and L. Venkataraman, *Nano Lett.*, 2020, **20**, 3320–3325.

26 J. A. Molina, F. J. Jiménez-Jiménez, P. Gómez, C. Vargas, J. A. Navarro, M. Orti-Pareja, T. Gasalla, J. Benito-León, F. Bermejo and J. Arenas, *J. Neurol. Sci.*, 1997, **150**, 123–127.

27 P. Hohenberg and W. Kohn, *Phys. Rev.*, 1964, **136**, B864–B871.

28 W. Kohn and L. J. Sham, *Phys. Rev.*, 1965, **140**, A1133–A1138.

29 A. K. Rappe, C. J. Casewit, K. S. Colwell, W. A. Goddard III and W. M. Skiff, *J. Am. Chem. Soc.*, 1992, **114**, 10024–10035.

30 M. D. Hanwell, D. E. Curtis, D. C. Lonie, T. Vandermeersch, E. Zurek and G. R. Hutchison, *J. Cheminf.*, 2012, **4**, 17.

31 M. J. Frisch, G. W. Trucks, H. B. Schlegel, G. E. Scuseria, M. A. Robb, J. R. Cheeseman, G. Scalmani, V. Barone, G. A. Petersson, H. Nakatsuji, X. Li, M. Caricato, A. V. Marenich, J. Bloino, B. G. Janesko, R. Gomperts, B. Mennucci, H. P. Hratchian, J. V. Ortiz, A. F. Izmaylov, J. L. Sonnenberg, D. Williams-Young, F. Ding, F. Lipparini, F. Egidi, J. Goings, B. Peng, A. Petrone, T. Henderson, D. Ranasinghe, V. G. Zakrzewski, J. Gao, N. Rega, G. Zheng, W. Liang, M. Hada, M. Ehara, K. Toyota, R. Fukuda, J. Hasegawa, M. Ishida, T. Nakajima, Y. Honda, O. Kitao, H. Nakai, T. Vreven, K. Throssell, J. A. Montgomery Jr, J. E. Peralta, F. Ogliaro, M. J. Bearpark, J. J. Heyd, E. N. Brothers, K. N. Kudin, V. N. Staroverov, T. A. Keith,

R. Kobayashi, J. Normand, K. Raghavachari, A. P. Rendell, J. C. Burant, S. S. Iyengar, J. Tomasi, M. Cossi, J. M. Millam, M. Klene, C. Adamo, R. Cammi, J. W. Ochterski, R. L. Martin, K. Morokuma, O. Farkas, J. B. Foresman and D. J. Fox, *Gaussian 16 Revision C.02*, 2019.

32 J.-D. Chai and M. Head-Gordon, *Phys. Chem. Chem. Phys.*, 2008, **10**, 6615–6620.

33 F. Weigend and R. Ahlrichsb, *Phys. Chem. Chem. Phys.*, 2005, **7**, 3297–3305.

34 F. Weigend, *Phys. Chem. Chem. Phys.*, 2006, **8**, 1057–1065.

35 J. Tomasi, B. Mennucci and R. Cammi, *Chem. Rev.*, 2005, **105**, 2999–3093.

36 A. V. Marenich, C. J. Cramer and D. G. Truhlar, *J. Phys. Chem. B*, 2009, **113**, 6378–6396.

37 E. Gorenskaia and P. J. Low, *Chem. Sci.*, 2024, **15**, 9510–9556.

38 R. Ramachandran, H. B. Li, W.-Y. Lo, A. Neshchadin, L. Yu and J. Hihath, *Nano Lett.*, 2018, **18**, 6638–6644.

39 M. Yaguchi, T. Uchida, K. Motobayashi and M. Osawa, *J. Phys. Chem. Lett.*, 2016, **7**, 3097–3102.

40 S. Sangtarash, A. Vezzoli, H. Sadeghi, N. Ferri, H. O'Brien, I. Grace, L. Bouffier, S. Higgins, R. Nichols and C. Lambert, *Nanoscale*, 2017, **10**, 3060–3067.

41 M. Di Ventra, S. T. Pantelides and N. D. Lang, *Phys. Rev. Lett.*, 2000, **84**, 979–982.

42 Y. Xue, S. Datta and M. A. Ratner, *Chem. Phys.*, 2002, **281**, 151–170.

43 F. Chen, X. Li, J. Hihath, Z. Huang and N. Tao, *J. Am. Chem. Soc.*, 2006, **128**, 15874–15881.

44 A. Kundu, B. Fingerhut and T. Elsaesser, *J. Chem. Phys.*, 2024, **161**, 084503.

45 M. Kiguchi, O. Tal, S. Wohlthat, F. Pauly, M. Krieger, D. Djukic, J. C. Cuevas and J. M. van Ruitenbeek, *Phys. Rev. Lett.*, 2008, **101**, 046801.

46 C. A. Martin, D. Ding, J. K. Sørensen, T. Bjørnholm, J. M. van Ruitenbeek and H. S. J. van der Zant, *J. Am. Chem. Soc.*, 2008, **130**, 13198–13199.

47 A. Borges, J. Xia, S. H. Liu, L. Venkataraman and G. C. Solomon, *Nano Lett.*, 2017, **17**, 4436–4442.

48 K. Homma, S. Kaneko, K. Tsukagoshi and T. Nishino, *J. Am. Chem. Soc.*, 2023, **145**, 15788–15795.

49 Y. Zhao, B. Ashcroft, P. Zhang, H. Liu, S. Sen, W. Song, J. Im, B. Gyarfas, S. Manna, S. Biswas, C. Borges and S. Lindsay, *Nat. Nanotechnol.*, 2014, **9**, 466–473.

50 R. G. Amorim, F. C. Lima, F. A. L. de Souza, W. L. Scopel, J. Prasongkit and R. H. Scheicher, *Nanoscale*, 2025, **17**, 2498–2505.

51 M. Vanzan, A. Migliore, M. Blanco-Formoso, F. De Angelis and S. Corni, *Nanoscale*, 2026, **18**, 5033–5051.

52 W. Shi, J. E. Greenwald and L. Venkataraman, *Nano Lett.*, 2024, **24**, 9283–9288.